Assessment of 3D Micro-Computed Tomography for PV Interconnection Technology Development

Rik Van Dyck [a,b,c,d *], Alexandros Prapavesis[a], Tom Borgers [b,c,d], Jonathan Govaerts [b,c,d], Jef Poortmans [b,c,d,e], Aart W. van Vuure [a]

a. KU Leuven, Department of Materials Engineering, Kasteelpark Arenberg 10, 3001 Leuven, Belgium
b. Hasselt University, imo-imomec, Martelarenlaan 42, 3500 Hasselt, Belgium
c. imec, imo-imomec, Thor Park 8320, 3600 Genk, Belgium
d. EnergyVille, imo-imomec, Thor Park 8320, 3600 Genk, Belgium
e. KU Leuven, Department of Electrical Engineering, Kasteelpark Arenberg 44, 3001 Leuven, Belgium

ARTICLE INFO

Keywords:
PV Module Characterization,
Micro-Computed Tomography,
Scanning Electron Microscopy,
Solder Joints,

ABSTRACT

X-ray (micro-)computed tomography is a non-destructive characterization method using photons to obtain multiple radiographic projections, which generates a 3D volume rendering of a scanned object after reconstruction. It is recently used in the research and development of photovoltaic modules to investigate smaller volumes in a PV module, for example, detection of cavities in solder joints and visualization of module volumes up to connection ribbon sizes. This work shows that current advanced devices are able to scan larger volumes, using a single-cell 20×20×0.5 cm^3 module with back-contact multi-ribbon interconnection technology as an example. The generated 3D volume renderings show the interconnection structures and give information on ribbon-metalization interconnections. Next to this, also the solder reflow volume is visible, indicating that the technology has great potential to be used in further interconnection technology development. Finally, a destructive cross section analysis using scanning electron microscopy is performed; it has a higher resolution and can differentiate elements with similar photon absorption coefficients, thus enabling microstructure and intermetallic compound analysis. The findings show the potential for micro-computed tomography as a non-destructive and relatively fast visualization method and how it can give complementary information to other characterization techniques for photovoltaic interconnection research.

* Corresponding author EnergyVille, imo-imomec, Thor Park 8320, 3600 Genk, Belgium
E-mail adress: rik.vandyck@imec.be (R. Van Dyck)

1 Introduction

The focus of silicon-based photovoltaic (PV) technology is shifting from increasing solar cell efficiency to developing novel interconnection and module concepts, aiming to improve module performance and overall system reliability. Development of new concepts usually starts with fabricating sample-sized modules, which are then subjected to reliability tests. Depending on the application, e.g. terrestrial usage, space PV, and vehicle- or building-integrated PV, the modules are exposed to different reliability tests such as temperature cycles, humidity and UV exposure or mechanical loading. During this phase, initial and intermediate evaluation is mainly based on both electrical and visual inspection. The former consists of electroluminescence (EL) imaging and current-voltage (I-V) characterization. The latter usually consists of a cross section analysis with optical or scanning electron microscopy (SEM), possibly supplemented by EDX or Raman spectroscopy mapping.

The cross section analysis requires time-consuming sample preparation and carries an additional risk of undesirable damage as a result of sample preparation. Although it yields high-resolution images, it only provides information on one 2D plane of the studied location in the module. In addition, it is rather destructive to the sample under consideration, which means that it can only be used as a final characterization method.

Non-destructive but less commonly used inspection methods in PV research include scanning acoustic microscopy (SAM) [1], [2] and micro-computed tomography (µCT) [3], [4]. SAM has proven to be suited for the detection of failure modes such as delamination and undesired voids in a broad range of research fields, including PV [1], [2], [5], [6]. Its resolution depends on the material and dimension of the scanned object, with high frequency scanning reaching resolutions lower than 40 µm [7]. However, it lacks the ability to generate 3D volumetric renderings of solder joints, cell metallization print, and other interconnection structures. By overcoming this limitation, µCT has the great potential to be used as a visual evaluation technique, which is especially important for the development of modules with more complex interconnections, such as shingling [8] multi-ribbon [9], multi-wire [10], [11], or foil-based approaches [12].

µCT was already introduced as a new diagnostic tool for the development of PV module technologies [13] Also, it is further used to inspect modules using the conductive backsheet approach for back-contact solar cells at the Energy Research Centre of the Netherlands (ECN) [14]. Solder joint analysis, using the technique is also being carried out but still limits itself to small-scale scanning of single solder joints [15]. Further elaboration of µCT applications in PV research is still required, in particular, due to newer lab-scale scanning devices with better performance for scanning larger-scale samples. These improvements include hardware upgrades offering more powerful X-ray energy source levels in order to achieve high penetration and perform tomography with increased signal-to-noise ratio, especially when the size of the inspection area is rather a few centimetres, as well as detectors with higher resolution scanning at faster acquisition times [16]. Along with hardware upgrades, the image reconstruction and post-processing algorithms have undergone strong improvements, particularly in terms of enhanced artefact compensation methods of high attenuation objects, such as metals, which are often problematic in µCT [17], [18] and are present in PV modules.

This work attempts to implement and further investigate how industrial µCT can benefit PV research with a module with three-dimensional multi-ribbon interconnection as an object of study [19]. A one-cell module was fabricated and electrically characterized using EL imaging and I-V characterization before, during, and after reliability testing. µCT scanning was performed on this module, and the reconstructed module volumes were analysed and visualized using the Avizo software. Next, a one-cell module using a multi-wire interconnection was scanned to show how this technique can be used for different module interconnection technologies. Finally, a cross section analysis using SEM was performed to compare and evaluate these visualization techniques.

2 Materials and Methods

2.1 Module sample preparation

Previous publications reported on a multi-ribbon interconnection for back-contact solar cells based on a 3D woven fabric of interconnection ribbons in an encapsulant matrix [19]. Reliability tests on sample-sized modules have shown the potential of this technology [20], but further tests on the fabrication processes are required to support the industrial development of the concept. Especially the solder joint formation is an essential aspect in evaluating its novel combined soldering and lamination approach. For this reason, a sample-sized module with ZEBRA interdigitated back-contact (IBC) cell using this interconnection technology, will be used as an object

of study in this work. The rear metalization design of the M6 ZEBRA IBC cell is shown in **Fig. 1**. It consists of continuous metal fingers that are alternately printed onto the positive and negative contacts of the junction on the back of the cell, with a finger pitch of 1.1 mm. At specific locations, a 10 µm thick insulation layer is printed on these metal fingers, covering either the positive or negative fingers, as illustrated in **Fig. 1(b)**. The alignment of a connecting electrically conductive ribbon across this insulation will therefore only address fingers of one electrical polarity.

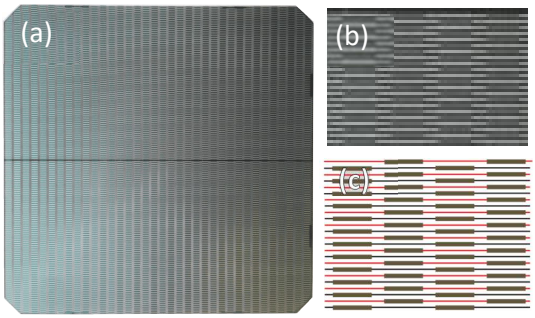

Fig. 1. Test **(a)** Picture and **(b)** zoomed-in picture of the rear metallization design of the used ZEBRA IBC cell. (c) Schematic drawing of the metallization, with the red and black horizontal lines as positive and negative fingers, respectively. The brown rectangles indicating the locations of the printed insulator

The one-cell module is fabricated using a two-step process involving a lay-up and lamination phase[19]. It consists of 2 mm thick glass front- and backsheets, an encapsulant between the front sheet and the cells, and a 420 µm thick glass-fiber reinforced thermoplastic polyolefin encapsulant with integrated interconnection ribbons between the backside of the cell and the backsheet. The interconnection ribbons have a 0.8 x 0.07 mm^2 copper core and are coated with a 5 to 25 µm thick layer of near eutectic Sn58Bi0.5Ag solder. The ribbons are directly soldered to the fingers in a combined soldering and encapsulation process in a vacuum laminator. Before soldering, a no clean flux is applied to the ribbons. An image of the front- and backside of the one-cell module is given in **Fig. 2**.

2.2 Reliability testing procedure

First, the sample was electrically characterized using EL imaging and I-V measurements. Reliability experiments were performed in the form of thermal cycling (TC) and humidity-freeze (HF) according to the IEC61215 standard [21]. The I-V characteristics of the module was measured at standard testing conditions (25°C, 1000W/m^2, AM1.5) at fixed intervals during the experiments. EL-images where captured with an exposure time of 3 seconds while an electrical current of 8 A was applied to the module. A total of 550 thermal cycles and 16 humidity-freeze cycles were performed.

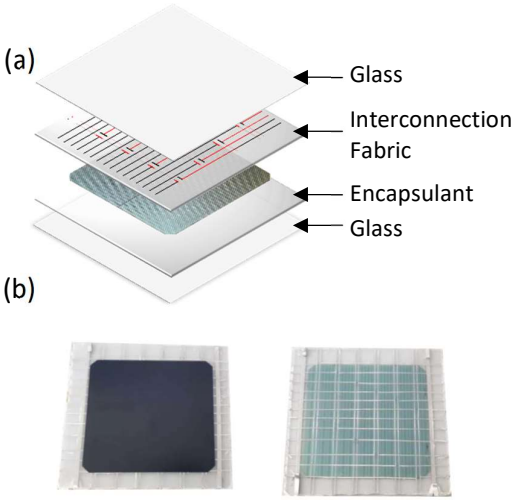

Fig. 2. (a) Exploded view of the the module during the layup phase of the fabrication, with, from top to bottom, frontsheet, encapsulant with integrated ribbons, sunny side facing down solar cell, front encapsulant and frontsheet . **(b)** Front- (Left) and backside (Right) of the one-cell sample module using the 3D multi-ribbon interconnection.

2.3 Micro-computed tomography

Micro-CT analysis was performed with an XL scanner, equipped with a 230 kV, 300 W microfocus X-ray tube with a tungsten reflection target, and with a 2856 × 2856 pixels detector with a 150 µm pixel pitch. The scans were performed at 230 kV and 50 W with a voxel size of 25 µm while 2×2-pixel binning was enabled on the detector, thus resulting in a 50 µm voxel size. Binning is a technique in which the charge for several pixels on the detector is added together. 2×2-pixel binning results in a doubling of the voxel size, but with a trade-off in a better signal-to-noise ratio, shorter exposure times, smaller projections, and faster reconstruction of datasets, which leads to higher quality images. Furthermore, a 1 mm thick metal beam filter was installed on the source to remove the longer-wavelength (or 'soft') part of the polychromatic X-ray spectrum. This reduces artifacts like photon scattering and beam hardening. Both copper and tin filters were tested. The tin filter was found to be more effective, whereas it was used for our experiments. In total, 2600 radiographic projections were acquired during a 360º angle sample rotation, each with an exposure time of 420 ms and a frame averaging set of 5, reducing the random noise. The total acquisition time was 86

minutes. The cross-sectional image reconstruction was then performed by applying a filter back-projection algorithm in the TESCAN reconstruction software Panthera. The results analysis and visualization were performed in the Avizo v2021 software.

2.4 Cross section analysis with scanning electron microscopy

A water-cooled diamond sawblade is used to cut 2×2 cm^2 pieces out of the module. After embedding the samples in an epoxy resin, and grinding and polishing the surface of the cross section, images were captured using a Tescan Vega SEM with acceleration potential of 15 kV and a back-scattered electron detector.

3 Results and Discussion

3.1 Reliability testing

Fig. 4. Graph showing the pseudo-fill factor (pFF) and fill factor (FF) of the one-cell module during thermal cycling (TC) and humidity-freeze (HF) reliability testing. TCX – HFY refers to the sample after X thermal cycles and Y humidity-freeze cycles. shows the I-V measurement results of the module at various stages during the reliability testing. A low initial fill factor (FF) would indicate either a high series resistance or a short circuit (shunt). The pseudo–fill factor (pFF) is also low, which implies that there is most likely a shunt in the module, causing the low *FF*.

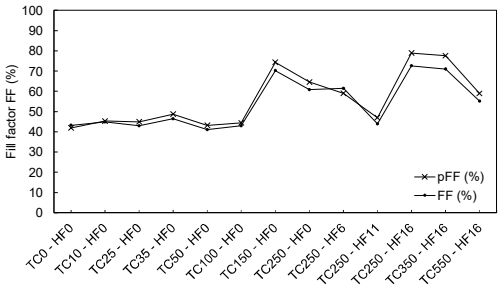

Fig. 4. Graph showing the pseudo-fill factor (pFF) and fill factor (FF) of the one-cell module during thermal cycling (TC) and humidity-freeze (HF) reliability testing. TCX – HFY refers to the sample after X thermal cycles and Y humidity-freeze cycles.

The EL images of the module at six stages during the reliability testing are given in **Fig. 3**. As the *FF* and *pFF* from the I-V measurements suggest, there is no significant change in the module performance during the first 100 thermal cycles. The first two EL images confirm this. Another 50 TC seems to cause an improvement of the performance as both *FF* and *pFF* increase, potentially as a result of the shunt being removed due to internal thermomechanical strain generated during thermal cycling. Another 100 TC and 11 HF cycles again reduce the *pFF* and *FF* to close to the initial values. The EL image also shows this drop in performance. This increase and decrease in performance is repeated in the last thermal and HF cycles, as indicated in both the I-V measurements and EL images. Although one could argue that the sample is inappropriate for further tests since it generates unpredictable results, this unstable shunt offers an opportunity to test the capabilities of µCT scanning. A dark area on the EL image is visible at the lower left corner of the module, potentially a result of a disconnected finger.

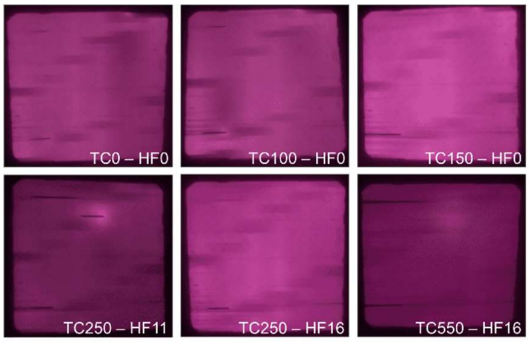

Fig. 3. Qualitative electroluminescence (EL) images of the one-cell module at different stages during reliability testing.

3.2 Micro-computed tomography

Reconstruction of the 3D volume renderings starts by defining the voxel histogram limits to only visualize the metal structures. **Fig. 5(a)** shows an example 3D volume rendering of the µCT scan on a part of the module, where numbers (1) and (2) indicate zoom-in locations for figures **Fig. 5 (b)** and **Fig. 5 (c),**

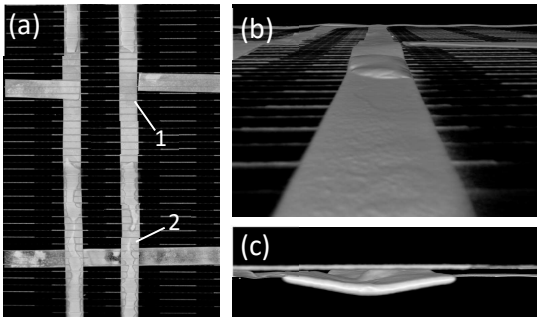

Fig. 5. 3D volume renderings of a µCT scan, in which the ribbon width of 0.8 mm can be used as a reference. **(a)** Volume rendering on part of the module, with interconnection ribbons and cell metallization. **(b)** Visualization of the ribbon-ribbon disconnection at location 1, and **(c)** Visualization of the ribbon-finger disconnection at location 2.

respectively. A ribbon-ribbon disconnection is visible at location (1). Due to the 3D nature of the scan, it is possible to observe these structures from different angles for further inspection. While the disconnection in **Fig. 5 (b)** was visible from the larger overview image, and potentially could be observed with an optical microsope, µCT can also show smaller disconnection flaws. An example is the ribbon-finger disconnection, shown in **Fig. 5 (c)**, which is in line with the observations in the EL images and confirms that µCT is able to visualize these smaller disconnections.

Fig. 6 shows a 3D volume rendering in which the location of a short circuit is indicated with a white circle. The thin insulation print is not visible due to the voxel size being larger than one-third of the insulation layer thickness. This means that the ribbon seems to be fully connected to the finger of the opposite polarity, which is not the case. However, a short circuit is still present and was observed in the volume renderings. As indicated by the circle, solder has flown next to the insulation print and formed a connection between the ribbon and a finger of opposite electrical polarity. This module defect was not observed with the naked eye or optical microscope. Performing cross section analysis using SEM to find the short circuit would be challenging because each analysis can only visualize one cross section, hence chances of actually finding the defect would be low.

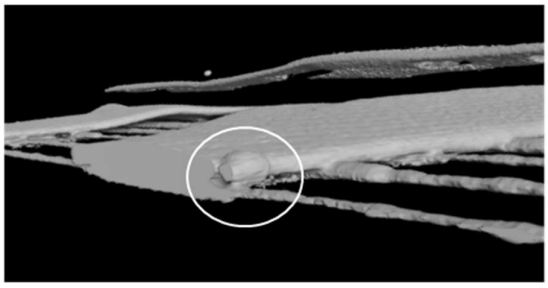

Fig. 6. Volume rendering showing a location where solder is connecting a ribbon and finger with opposite electrical polarity, creating a short circuit in the module. The ribbons are 0.8 mm wide and the finger pitch is 1.1 mm.

Fig. 7 shows an image of a volume rendering where two parallel ribbons are soldered on the cell metallization. The information obtained from this µCT image goes beyond disconnection failure detection. The solder reflow volume is visual; in this case, the solder is mainly concentrated in the transversal middle part of the ribbons, spreading evenly in the longitudinal direction. Such information can be interesting for various aspects of PV interconnection development. First, it can indicate whether the soldering process is effective, which is especially important for novel interconnection methods using shingling, multi-wire, or combined soldering and encapsulation approaches. Secondly, the volume renderings give a better idea of the actual shape of the solder joint compared to a 2D image obtained from a cross section analysis. This information can also be used to generate a 3D-mesh structure of the solder joint for finite element modelling of the module interconnection technologies [22].

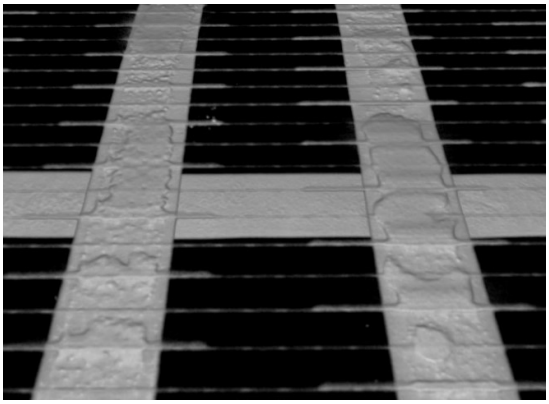

Fig. 7. Two parallel, 0.8 mm wide ribbons soldered to the cell metallization (fingers). The solder volume is slightly concentrated in the centre of the ribbons.

Photon scattering is one of the artefacts that can reduce image quality and is increased by volumes with high metal concentrations. For this reason, back contact modules are the most challenging to scan because all metal structures are at one side of the Si cell. **Fig. 8** shows a volume rendering image for a module using a two-sided multi-wire interconnection, where the wires are directly soldered onto the fingers of the cell. This scan indicates that the technique can also be used in the development of other interconnection methods, while having less photon scattering, thus higher image quality. Although analysing these images and the 3D volumes renderings using the Avizo software gives insight into the actual interconnection structure and solder joint shapes, µCT still leaves some questions unanswered. The high X-ray photon absorption by the metal imposes a need for high voltages, making it difficult to analyse the other module materials. With the used relatively large-scale scanning equipment, the resolution turned out to be limited to a few µm, making the observation of smaller cavities or solder structures impossible. Finally, the matching absorption coefficients for the different metals in the solder alloy, interconnection ribbons, and cell metallization make it impossible to identify them with varying voxel intensities. If these aspects are of

interest, a destructive cross section analysis using SEM is still preferred.

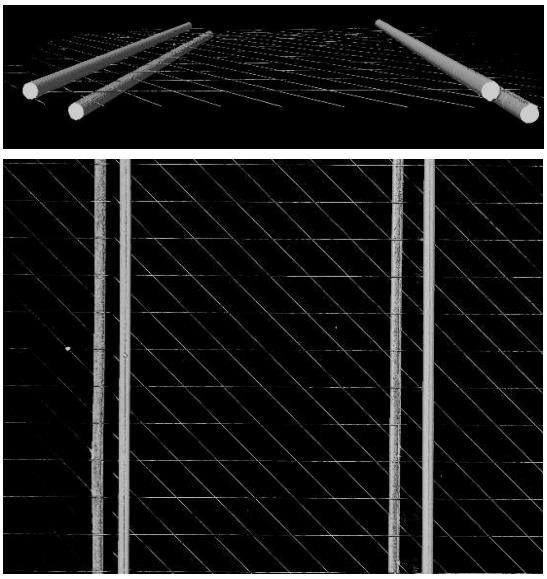

Fig. 8. 3D volume renderings of a module with multi-wire interconnection. The 250 µm thick wires and cell metalization (fingers) are visible.

3.3 Cross section analysis using SEM

Using a back-scattered electron detector, SEM images were acquired from cross sections of the studied sample-sized module. **Fig. 9 (a)** shows a cross section in the transverse direction of the ribbon. As observed in the µCT scans, the solder is mainly situated in the middle of the ribbon. **Fig. 9 (b)** shows a cross section in the longitudinal direction. The solder is evenly spread over the length of the ribbon, which is in line with the findings from the µCT scanning. However, the SEM resolution is higher; hence the thin insulation between the finger cell is visible. This is shown in a zoomed image in **Fig. 9 (c).**

Since the back-scattering of electrons depends on the atomic weight of the samples' materials, a cross section analysis can give information on the metal phase distribution in the solder joint. This is especially important in the search for lead-free solder alloys for PV applications. The zoomed image in **Fig. 10** shows an intensity difference between the Cu ribbon, Bi-rich, and Sn-rich phases. The intermetallic compound (IMC) layer is visible as a slightly lighter grey area around the Cu ribbon. Its scallop-like structure indicates that Cu_6Sn_5 is present. Determining the thickness and structure of this IMC layer are essential aspects of evaluating the solder joint formation and they have a significant impact on the solder joint reliability [23].

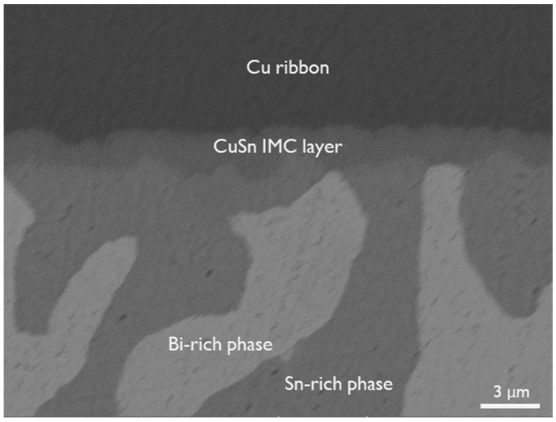

Fig. 10. Scanning electron microscopy image using back-scattered electrons showing different metal phases of a solder joint.

4 Conclusions

In this work, state-of-the-art µCT scanning devices were able to construct 3D volume renderings of sample-sized PV modules. They show the advances made within the µCT research field and demonstrate that it can be an additional visual inspection technique for module technology development. It can analyse solder joint reflow volume and the interconnection structure. This is complementary to the higher resolution of a cross section analysis using SEM, which can also detect and distinguish different metals within the module. In this sense, combining 3D µCT and SEM imaging leads to more reasoned evaluations

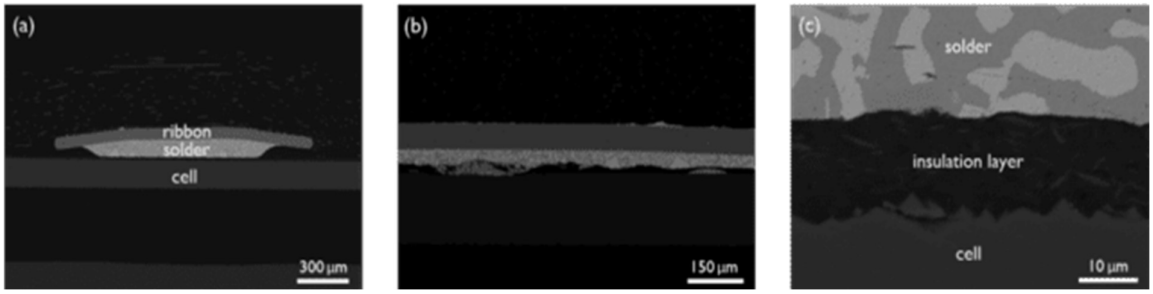

Fig. 9. Scanning electron microscopy images of a cross section in **(a)** transverse and **(b)** longitudinal direction of the interconnection ribbons. **(c)** Zoomed-in image showing a thin insulation layer between the cell and the solder alloy.

and conclusions for the visual inspection of PV modules in research. Latest developments in µCT scanning devices include a photon-counting spectral detector, enabling an inherent quantitative chemical analysis similar to SEM.

Acknowledgments

The authors gratefully acknowledge imec's SiPV industrial affiliation programme and its partners, Fonds Wetenschappelijk Onderzoek, through the SB Ph.D. Fellowship under grant number 1S14120N, and their large infrastructure I013518N project for the financial support of the X-ray infrastructure. The KU Leuven XCT Core facility is acknowledged for the 3D image acquisition and quantitative post-processing tools (https://xct.kuleuven.be/), and ISC Konstanz for providing the IBC solar cells.

Data Availability

The data that support the findings of this study are available from the corresponding author upon request.

Authors Contribution

Rik Van Dyck: Conceptualization, Methodology, Investigation, Writing-Original draft preparation **Alexandros Prapavesis:** Software**,** Investigation, Methodology, Writing-Review & Editing **Tom Borgers:** Investigation, Writing-Review & Editing. **Jonathan Govaerts:** Investigation, Writing-Review & Editing **Jef Poortmans:** Writing-Review & Editing, Supervision **Aart W. van Vuure:** Writing-Review & Editing**,** Supervision

References

[1] K. Dressler *et al.*, "Characterisation of Rear Local Contacts Including BSF Formation Using Raman and Scanning Acoustic Microscopy," in *27th EUPVSEC*, 2012, pp. 755–758.

[2] D. E. Mansour, S. Kotterer, D. Philipp, and P. Gebhardt, "PV Backsheet Failure Analysis by Scanning Acoustic Microscopy," in *37th EUPVSEC*, 2020, pp. 1014–1018.

[3] K. Dressler, M. Rauer, M. Kaloudis, S. Dauwe, A. Herguth, and G. Hahn, "Nondestructive Characterization of Voids in Rear Local Contacts of PERC-Type Solar Cells,"*,IEEE Journal of Photovoltaics*, vol. 5, pp. 70–76, 2015, doi: 10.1109/JPHOTOV.2014.2359745.

[4] A. de Rose, T. Geipel, D. Eberlein, A. Kraft, and M. Nowottnick, "Interconnection of Silicon Heterojunction Solar Cells by Infrared Soldering-Solder Joint Analysis and Temperature Study," in *36th EUPVSEC*, 2019, pp. 229–234.

[5] F. Bertocci, A. Grandoni, and T. Djuric-Rissner, "Scanning acoustic microscopy (SAM): A robust method for defect detection during the manufacturing process of ultrasound probes for medical imaging," *Sensors*, vol. 19, no. 4868, 2019, doi: 10.3390/s19224868.

[6] S.-L. Gao and J.-K. Kim, "Scanning acoustic microscopy as a tool for quantitative characterisation of damage in CFRPs," *Composites Science Technology*, vol. 59, pp. 345–354, 1999. doi:10.1016/S0266-3538(98)00086-4

[7] T. Tamulevičius *et al.*, "Micromachining and validation of the scanning acoustic microscope spatial resolution and sensitivity calibration block for 20–230 MHz frequency range," *Microscopy*, vol. 65, no. 5, pp. 429–437, 2016, doi: 10.1093/jmicro/dfw027.

[8] D. Tonini, G. Cellere, M. Bertazzo, A. Fecchio, L. Cerasti, and M. Galiazzo, "Shingling technology for cell interconnection: Technological aspects and process integration," in *Energy Procedia*, 2018, vol. 150, pp. 36–43. doi: 10.1016/j.egypro.2018.09.010.

[9] S. Braun, G. Hahn, R. Nissler, C. Pönisch, and D. Habermann, "Multi-busbar solar cells and modules: High efficiencies and low silver consumption," in *3rd International conference on Silicon Photovoltaics*, 2013, vol. 38, pp. 334–339. doi: 10.1016/j.egypro.2013.07.286.

[10] J. Walter, M. Tranitz, M. Volk, C. Ebert, and U. Eitner, "Multi-wire interconnection of busbar-free solar cells," in *4th International conference on Silicon Photovoltaics*, 2014, vol. 55, pp. 380–388. doi: 10.1016/j.egypro.2014.08.109.

[11] T. Borgers, E. Voroshazi, J. Govaerts, J. Szlufcik, and J. Poortmans, "Multi-wire interconnection technologies weaving the way

for back contact and bifacial PV modules," in *IEEE PVSEC*, 2016, pp. 3580–3583. doi: 10.1109/PVSC.2016.7750339.

[12] I. J. Bennett, M. J. A. A. Goris, and W. Eerenstein, "Reducing the Cost Of MWT Module Technology Based on Conductive Back-Sheet Foils," in *28th EUPVSEC*, 2013, pp. 3111–3113.

[13] E. C. Quintana, M. A. Quintana, K. D. Rolfe, K. R. Thompson, and P. Hacke, "Exploring diagnostic capabilities for application to new photovoltaic technologies," in *IEEE PVC*, 2009, pp. 002031–002036. doi: 10.1109/PVSC.2009.5411471.

[14] D. Veldman, I. J. Bennett, B. Brockholz, and P. C. de Jong, "Non-destructive testing of crystalline silicon photovoltaic back-contact modules," in *Energy Procedia*, 2011, vol. 8, pp. 377–383. doi: 10.1016/j.egypro.2011.06.153.

[15] N. H. Jabarullah, A. Surendar, M. Arun, A. F. Siddiqi, and T. Krasnopevtseva, "Microstructural Characterization and Unified Reliability Assessment of Aged Solder Joints in a PV Module," *IEEE Transactions on Components, Packaging and Manufacturing Technologyl*, vol. 10, no. 6, pp. 1028–1034, 2020, doi: 10.1109/TCPMT.2020.2972027.

[16] W. Sun *et al.*, "Review of high energy X-ray computed tomography for non-destructive dimensional metrology of large metallic advanced manufactured components," *Reports on Progress in Physics*, vol. 85, no. 1. , 2022. doi: 10.1088/1361-6633/ac43f6.

[17] X. Zhang, J. Wang, and L. Xing, "Metal artifact reduction in x-ray computed tomography (CT) by constrained optimization," *Medical Physics*, vol. 38, no. 2, pp. 701–711, 2011, doi: 10.1118/1.3533711.

[18] N. G. Hokamp *et al.*, "Quantification of metal artifacts in computed tomography: Methodological considerations," *Quantitative Imaging in Medical Surgery*, vol. 10, no. 5, pp. 1033–1044, May 2020, doi: 10.21037/QIMS.2020.04.03.

[19] R. van Dyck, T. Borgers, J. Govaerts, J. Poortmans, and A. W. van Vuure, "Three-dimensional multi-ribbon interconnection for back-contact solar cells," *Progress in Photovoltaics: Research and Applications*, vol. 29, no. 5, pp. 507–515, 2021, doi: https://doi.org/10.1002/pip.3390.

[20] R. van Dyck *et al.*, "Three-Dimensional Multi-Ribbon Back-Contact Interconnection: Latest Results on Reliability Testing," in *38th EUPVSEC*, 2021, pp. 728–731.

[21] "IEC 61215-1 Terrestrial photovoltaic (PV) modules – Design qualification and type approval," 2021.

[22] P. Nivelle, J. A. Tsanakas, J. Poortmans, and M. Daenen, "Stress and strain within photovoltaic modules using the finite element method: A critical review," *Renewable and Sustainable Energy Reviews*, vol. 145, 2021, 111022. doi: 10.1016/j.rser.2021.111022.

[23] M. T. Zarmai and C. F. Oduoza, "Impact of inter-metallic compound thickness on thermo-mechanical reliability of solder joints in solar cell assembly," *Microelectronics Reliability*, vol. 116, 2021, 114008, doi: 10.1016/j.microrel.2020.114008.